nature communications

Article

https://doi.org/10.1038/s41467-024-50854-4

Reprogramming the myocardial infarction microenvironment with melanin-based composite nanomedicines in mice

Received: 21 March 2023

Accepted: 24 July 2024

Published online: 06 August 2024

Check for updates

Yamei Liu[1,2,8], Shuya Wang[3,4,8], Jiaxiong Zhang[1,2], Quan Sun[1,2], Yi Xiao[1,2], Jing Chen[1], Meilian Yao[1], Guogang Zhang[1,2,5], Qun Huang[6], Tianjiao Zhao[3,4], Qiong Huang[2,7], Xiaojing Shi[2,7], Can Feng[3], Kelong Ai[3,4] ✉ & Yongping Bai[1,2] ✉

Myocardial infarction (MI) has a 5-year mortality rate of more than 50% due to the lack of effective treatments. Interactions between cardiomyocytes and the MI microenvironment (MIM) can determine the progression and fate of infarcted myocardial tissue. Here, a specially designed Melanin-based composite nanomedicines (MCN) is developed to effectively treat MI by reprogramming the MIM. MCN is a nanocomposite composed of polydopamine (P), Prussian blue (PB) and cerium oxide (Ce_xO_y) with a Mayuan-like structure, which reprogramming the MIM by the efficient conversion of detrimental substances (H^+, reactive oxygen species, and hypoxia) into beneficial status (O_2 and H_2O). In coronary artery ligation and ischemia reperfusion models of male mice, intravenously injecting MCN specifically targets the damaged area, resulting in restoration of cardiac function. With its promising therapeutic effects, MCN constitutes a new agent for MI treatment and demonstrates potential for clinical application.

Myocardial infarction (MI) is the most emergent manifestation of cardiovascular disease. Cardiovascular diseases account for 1/3 of the annual global death toll[1]. Despite the substantial progress in the prevention of cardiovascular diseases in the past few decades, 50 million patients worldwide still experience MI each year[2]. Reperfusion is the only effective clinical approach to resolve ischemic injury, but upon reperfusion, myocardial tissue is replaced by fibrotic scars, leading to cardiac dysfunction and life-threatening complications[3]. MI frequently progresses to chronic heart failure (HF), resulting in a 5-year mortality rate greater than 50% after MI[4]. Various therapeutic approaches, such as cell transplantation, exosome treatment, and cardiac patch therapy, have been used for MI, with varying degrees of success[5]. However, therapeutic options to prevent, slow and reverse MI progression remain extremely limited. Therefore, effective approaches to treat MI and prevent its progression to HF are unmet but urgent needs.

The MI microenvironment (MIM) plays a crucial role in determining the fate of the affected myocardial tissue. The effective treatment and the prevention of its progression to HF depend on managing the complex interactions between cardiomyocytes and the MIM. Options for MI treatment and prevention remain limited, but ongoing research is aimed at improving outcomes for patients worldwide. Previous study has generally focused on manipulating biological

[1]Department of Geriatric Medicine, Coronary Circulation Center, Xiangya Hospital, Central South University, Changsha, Hunan, P.R. China. [2]National Clinical Research Center for Geriatric Disorders, Xiangya Hospital, Central South University, Changsha, Hunan, P.R. China. [3]Xiangya School of Pharmaceutical Sciences, Central South University, Changsha, Hunan, P.R. China. [4]Hunan Provincial Key Laboratory of Cardiovascular Research, Xiangya School of Pharmaceutical Sciences, Central South University, Changsha, Hunan, P.R. China. [5]Department of Cardiology, The Third Xiangya Hospital, Central South University, Changsha, Hunan, P.R. China. [6]Department of Child Health Care, Hunan Provincial Maternal and Child Health Care Hospital, Changsha 410008 Hunan, P.R. China. [7]Department of Pharmacy, Xiangya Hospital, Central South University, Changsha, Hunan, P.R. China. [8]These authors contributed equally: Yamei Liu, Shuya Wang. ✉e-mail: aikelong@csu.edu.cn; baiyongping@csu.edu.cn

factors such as inflammatory factors and key proteins in the MIM to treat MI[6]. The treatment of MI can be challenging due to the complex nature of the MIM. The MIM is composed of various components and factors that work together to establish a challenging environment in which to implement effective therapies. Moreover, it is important to consider the intricate connections among the various components and factors to effectively treat MI. Targeting a single biological factor may result in only limited and transient efficacy.

The MIM is formed due to the effects of physical and chemical parameters within the MI site, after which the infiltration of inflammatory cells and the secretion of various inflammatory mediators and profibrotic factors occur. The pH, O_2 concentration, and redox balance are crucial considerations in the treatment of MI. These three parameters are important contributors to the complexity of the MIM and greatly decrease the efficacy of therapeutic interventions. In addition, focusing on a single biological factor may be insufficient for the long-term treatment of MI; thus, a comprehensive approach is essential. Moreover, the MIM can change over time, and the presence of inflammatory cells and mediators can further complicate treatment[7]. Importantly, pH can significantly impact the functions of proteins. Even a small shift in pH can cause a major change in the surface charge of proteins, which can affect their function. This phenomenon is especially important in normal myocardial tissue, in which intracellular pH values must remain within a narrow range for the efficient activity of many cardiac signaling pathway. The ideal myocardial pH range is ~7.1–7.2[8]. However, hypoxia at the MI site drives a shift from fatty acid metabolism to anaerobic glycolysis, resulting in substantial production of lactic acid. This metabolic reprogramming, in turn, decreases the pH at the MI site, resulting in levels as low as 6.5–6.8[9]. Indeed, MI has a detrimental effect on cardiomyocyte mitochondria due to hypoxia within the myocardium. This hypoxic condition can cause excessive reactive oxygen species (ROS) production, which leads to a rapid change in the redox environment within the infarcted myocardial tissue. Ultimately, this change can result in the activation of apoptosis or other forms of cell death in cardiomyocytes[10]. Currently, there is considerable interest in adopting nanomedicines to modify the MIM, mostly by supplying O_2[11] or removing excess ROS[12]. However, thorough three-dimensional (pH, hypoxia, and ROS) studies on the MIM are lacking, although tripartite modification of the MIM may be the most promising therapeutic approach for improving the prognosis of MI patients. The main cause of this therapeutic bottleneck is the extreme difficulty of simultaneously reversing the adverse changes in pH, ROS, and oxygen content in situ.

In this work, we proposed and constructed a Melanin-based composite nanomedicines (MCN) that can efficiently convert harmful factors ((i.e., detrimental substances: H^+, ROS, and hypoxia) in the MIM into beneficial substances (i.e., beneficial elements: O_2 and H_2O), which may result in reprogramming of the MIM. MCN contains three components, namely, polydopamine nanospheres (P), Prussian blue (PB), and cerium oxide (Ce_xO_y), which form a mutually cooperative system at the nanoscale. MCN can subtly convert $O_2^{\bullet-}$, $^{\bullet}OH$, and H^+ into O_2 and H_2O in the MIM through three enzyme-catalyzed cascade reactions. Through a noninvasive intravenous injection route, MCN can be targeted to infarcted myocardial tissue with high specificity and demonstrate excellent myocardial repair effects by reprogramming the MIM. Due to its nanoscale size, MCN exhibits high specificity and is targeted toward the infarcted area upon administration via invasive intravenous injection. MCN reprograms the MIM and reverse MIM and reverses its dysregulation to restore homoeostasis, resulting in a reduction in cardiomyocyte apoptosis, the suppression of inflammatory factor releases and the promotion of M2 macrophage polarization. MCN has superior myocardial repair function and HF resistance due to this comprehensive effect.

Here, we synthesized MCN nanomedicine for converting key detrimental substances into beneficial status in the MIM. MCN specifically enriched in infarcted myocardial tissues and in the mitochondria of cardiomyocytes, restored homeostasis in the MIM, reduced mitochondrial ROS levels to protect the mitochondrial integrity and function, significantly inhibited cardiomyocyte apoptosis, and greatly reduced inflammation and fibrosis in infarcted myocardial tissues. In addition, MCN is composed of P (an endogenous substance in the body), PB (an agent that has been approved by the FDA for clinical treatment for decades)[13], and Ce_xO_y[14] at very low concentrations. Consistent with its composition, MCN does not exhibit any toxic side effects at therapeutic doses. Therefore, MCN has great clinical application prospects for MI and constitutes a paradigm for efficient targeted treatment of MI via remodeling of the MIM.

Results and discussion

Synthesis and characteristics of MCN

MCN was prepared by sequentially growing PB and Ce_xO_y on P NPs and then modifying the NPs with polyethylene glycol (PEG) (Fig. 1a). Compared with P NPs (Fig. S1a), MCN had a unique structure similar to Mayuan (a traditional Chinese delicacy, Fig. 1b inset) attributed to the in situ growth of PB and Ce_xO_y (Fig. 1b). The successful preparation of MCN was confirmed through systematic characterization ("Characteristics" section in the Supplemental Information (SI), Figs. S1–S5). Given the short transport distances (10^{-9} m) of the highly reactive ROS (such as $O_2^{\bullet-}$ and $^{\bullet}OH$), the proximity of the three key components (P, PB, and Ce_xO_y) in MCN at the nanoscale was important for the mutual synergy among the three cascade reactions (Fig. 1c). In our previous study[15], we revealed that P converts $O_2^{\bullet-}$ to H_2O_2 and OH^- through SOD-like enzymatic activity, after which OH^- and H^+ react to produce H_2O (Step 1). PB has two enzyme-like properties. On the one hand, PB converts H_2O_2 into H_2O and O_2 through its CAT-like enzymatic activity[16]. However, PB also has peroxidase (POD)-like enzymatic activity, through which it converts H_2O_2 into the more toxic $^{\bullet}OH$[17]. More importantly, these two enzymatic activities of PB are pH dependent, and its POD activity was increased in the acidic MIM (Step 2)[18]. Most importantly, Ce_xO_y on MCN converted $^{\bullet}OH$ to O_2 and H_2O through a two-step synergistic reaction (Step 3)[19]. Through these three closely coordinated cascade reactions, MCN efficiently converted ROS and H^+ into O_2 and H_2O. As shown in Fig. 1d and Figs. S6–S8, MCN had strong SOD-like enzymatic activity, similar to P and to PB grown separately on polydopamine nanoparticles (hereafter referred to as PP), as shown by the nitroblue tetrazolium assay, indicating that the PB and Ce_xO_y modifications did not impair the SOD-like enzymatic activity of P. We examined the $O_2^{\bullet-}$ metabolites and found that $O_2^{\bullet-}$ reacted readily with NO to produce the cytotoxic molecule $ONOO^-$[20]. The $ONOO^-$ scavenging ability of MCN was investigated with a pyrogallol assay. As shown in Figs. S9–S10, MCN had a strong ability to scavenge $ONOO^-$. $^{\bullet}OH$ production mediated by PP NPs and MCN was further evaluated with 3,3′,5,5′-tetramethylbenzidine (TMB) at pH 4 (similar to the lysosomal pH), pH 6.5 (similar to the MIM pH) and pH 7.4 (normal physiological pH). PP NPs catalyzed $^{\bullet}OH$ production even at neutral pH, and $^{\bullet}OH$ production increased with decreasing pH (Fig. 1e). As shown in Fig. 1f, MCN efficiently scavenged up to 63.94% of the $^{\bullet}OH$ content at pH 6.5. Moreover, the $^{\bullet}OH$ scavenging capacities of MCN at pH 4 (Fig. S11) and pH 7.4 (Fig. S12) were approximately 42.31% and 64.29%, respectively, indicating that MCN can effectively convert $^{\bullet}OH$ to O_2 under different pH conditions because of the Ce_xO_y on its surface. This ability is highly promising for the conversion of toxic H_2O_2 and $^{\bullet}OH$ into O_2, an event that can not only reduce ROS-mediated damage but also spontaneously generate O_2. As shown in Fig. 1g, h and Figs. S13, S14, MCN produced far more O_2 bubbles in the presence of H_2O_2, than did PP NP.

MI targeting ability and therapeutic effect of MCN

It was crucial to determine whether MCN can accumulate in the ischemic region. To facilitate this observation, MCN was modified with

https://doi.org/10.1038/s41467-024-50854-4

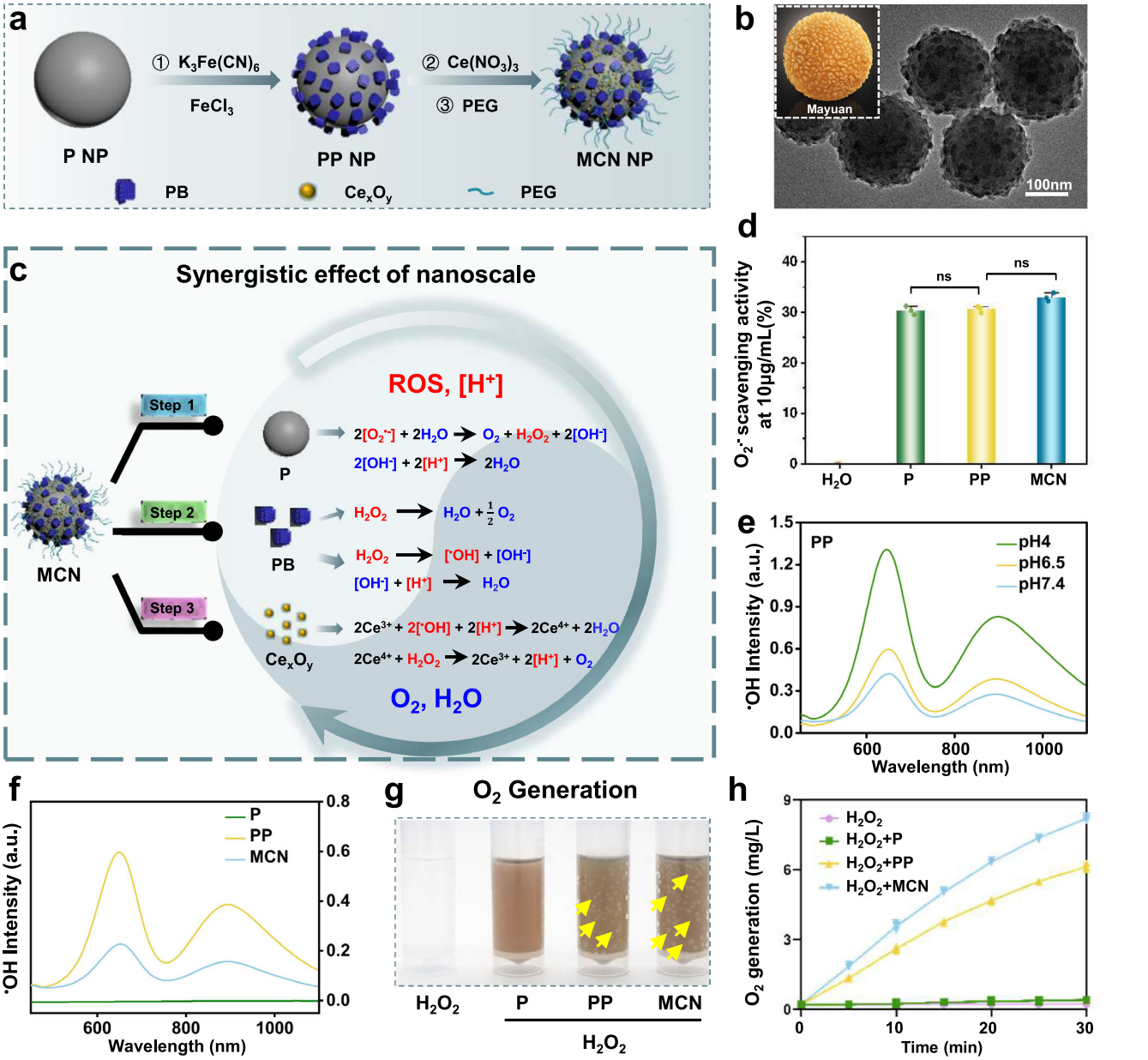

Fig. 1 | Characterization of MCN. a Diagram illustrating the synthesis process of MCN. **b** Transmission electron microscopy (TEM) visualizations of MCN with a scale bar representing 100 nm. The data were replicated across three distinct experiments. **c** Diagrammatic representation emphasizing the role of MCN in ameliorating hypoxic conditions. **d** $O_2^{\cdot-}$ scavenging activities in the presence of P, PP, or MCN. **e** ·OH production trends of PP NPs across pH values of 4, 6.5, and 7.4. **f** ·OH scavenging capacities of P, PP, or MCN, specifically at pH 6.5. **g** Augmented oxygen bubble formation (indicated by yellow arrows) in MCN at pH 6.5. **h** O_2 production profiles for H_2O_2, P, PP, or MCN. All presented data stems from mean ± SD, replicated across three distinct experiments. Three-or-more-group statistical significance was calculated by one-way ANOVA followed by Bonferroni post hoc correction. ns $P > 0.05$.

fluorescein isothiocyanate (generating MCN-FITC) to trace MCN accumulation. By transmission electron microscopy (TEM), we observed vascular destruction of the infarcted myocardial tissue; specifically, the vascular gap was as wide as 1.2 μm with a peak width of approximately 370 nm (Fig. 2a and Fig. S15)[21]. This feature made it possible for MCN to target the infarcted myocardial tissue. By energy-dispersive X-ray spectroscopy (EDS), we verified that MCN was enriched in the infarcted myocardial tissue (Fig. 2b). After intravenous injection of MCN-FITC, the fluorescence signal was stronger in the infarcted area than in the other organs in both the non-MI group and the MI group on Day 1 (Fig. 2c, d). MCN-FITC accumulated in the infarcted region with significant specificity of organ distribution (Fig. 2e and Fig. S16). Moreover, the concentration of cerium was 349.2 ± 48.32 ng/g in the MI tissues but 30.45 ± 14.07 ng/g in the healthy myocardium, indicating more than 10-fold enrichment, as determined by inductively coupled plasma mass spectrometry (ICP–MS) (Fig. S17). This finding was consistent with the results of our MCN-FITC uptake assay. More specifically, MCN-FITC was effectively taken up by cardiac endothelial cells, cardiac fibroblasts, cardiac macrophages, and cardiomyocytes under hypoxic conditions (Fig. S18). Moreover, MCN specifically targeted the infarcted area within ten minutes of administration (Fig. S19), and the fluorescence intensity and the amount of cerium exhibited the same trend, i.e., peaking the Day 1 after injection and then decreasing by approximately 1/2 of the initial values on Day 3 and by ~4/5 of the initial values on Day 7 (Fig. S20). These data indicate that the half-life of MCN is ~2.8 days (~3 days). Considering that the main damage caused by MI occurs during the first 7 days and considering the half-life of MCN, we

https://doi.org/10.1038/s41467-024-50854-4

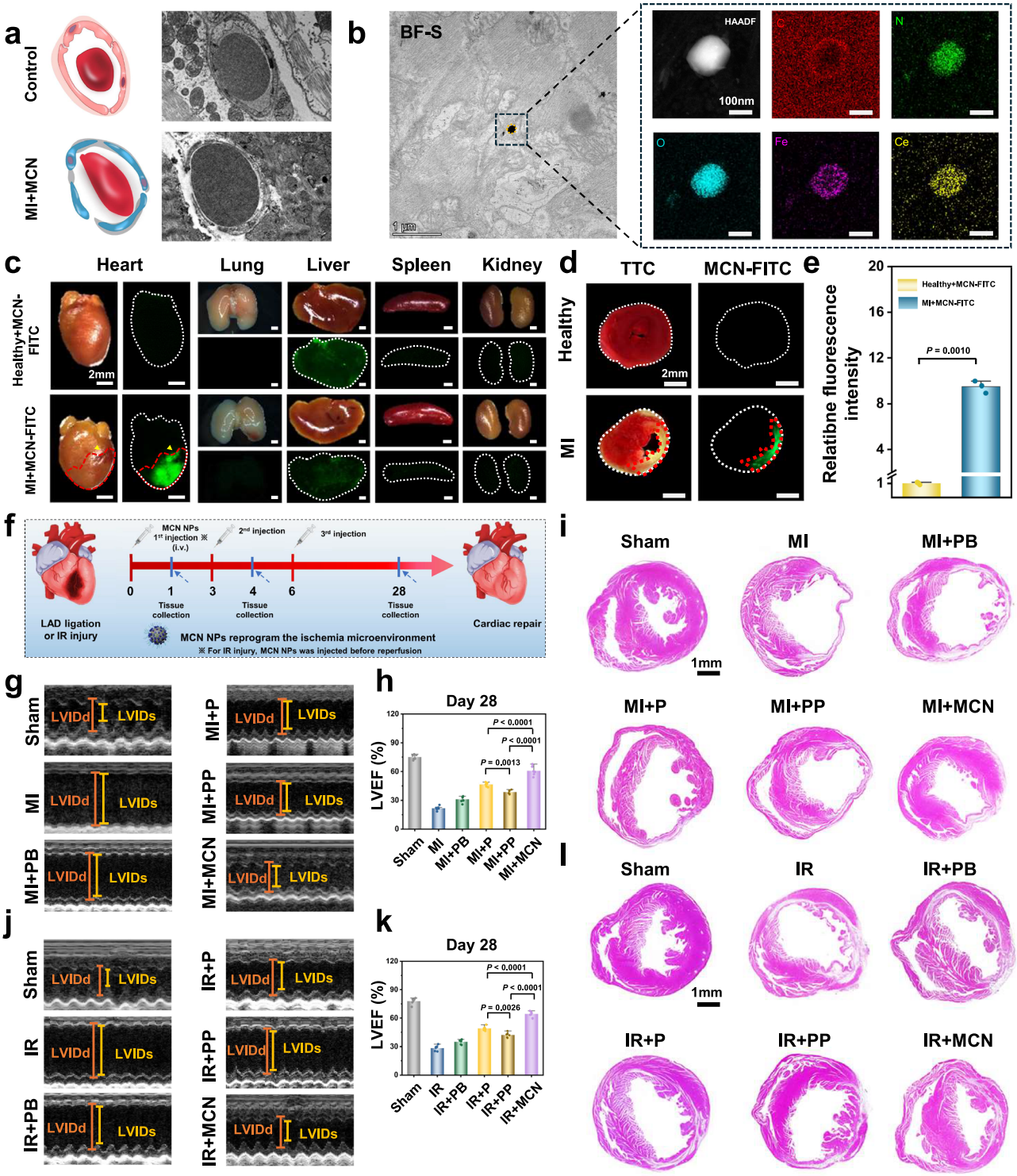

Fig. 2 | Distribution of MCN in vivo and the recovery of cardiac function after MCN treatment in MI and I/R injury model. a Representative TEM images of healthy vessels and infarcted vessels on day 1 after MI. **b** High-angle annular dark field (HAADF) STEM reveals the MCN localized on myocardial mitochondria of the infarct area (carbon, nitrogen, oxygen, iron, and cerium are abbreviated as C, N, O, Fe, and Ce separately). BF-S bright field-STEM. **c** Representative images of mice hearts of TTC staining and MCN-FITC NPs injection on day 1 after MI (the yellow triangle points to the LAD ligation site). **d** Quantitative fluorescence intensity data. **e** Fluorescence and bright field of mouse heart, lungs, liver, spleen, and kidneys post tail vein injection of NPs in healthy or MI mice ($n = 3$ mice per group). **f** Schematic image showing the MCN treatment of mouse heart after MI or ischemia-reperfusion injury (i.v. intravenous injection). **g** Characteristic echocardiography image after treatment with PB (positive control), P, PP, and MCN on day 28 after MI and quantitative analysis of LVEF (**h**) ($n = 6$ mice per group). **i** Representative images of HE's staining on day 28 after MI. **j** Characteristic echocardiography image after treatment with PB (positive control), P, PP, and MCN on day 28 after I/R injury and quantitative analysis of LVEF (**k**) ($n = 6$ mice per group). **l** Representative images of HE's staining on day 28 after I/R injury. Scale bar: 1 mm ($n = 6$ animals per group). All data were presented as the mean ± SD. Two-group statistical significance was calculated by unpaired two-tailed Student's *t*-test, and three-or-more-group statistical significance was calculated by one-way ANOVA followed by Bonferroni post hoc correction. Some of the drawing materials for Fig. 2f were downloaded from BioRender.com and are released under a Creative Commons Attribution-NonCommercial-NoDerivs 4.0 International license.

designed multiple injection plans (Fig. S21) and specific the dose (Fig. S22) of MCN, and finally chose MCN injection with day by next day and 7.5 mg/Kg as our subsequent dosage (Fig. 2f). Echocardiography is the gold standard for assessing cardiac function based on the left ventricular ejection fraction (LVEF)[22,23]. As shown in Fig. 2g–h, the LVEF was decreased to 22.74 ± 1.865% in the MI group. Neither P NP treatment nor PP NP treatment significantly reversed the decrease in the LVEF. Thus, we inferred that the PB in PP may produce toxic ·OH (with POD-like properties), which damages the heart. Interestingly, normal function of the post-MI heart was restored after MCN treatment, with an LVEF of 60.7 ± 5.013%, which was significantly higher than that in either the P or PP NP group and greater than that in tissue treated with a widely used positive control, PB NPs. The potent efficacy of MCN NPs was further confirmed by measurement of the left ventricular fractional shortening (LVFS), end-diastolic volume (EDV), end-systolic volume (ESV), left ventricular internal diameter end diastole (LVIDd) and left ventricular internal diameter end-systole (LVIDs) (Fig. S23). In addition, cardiac function in the MCN group progressively improved with increasing treatment time (Fig. S24). On Day 28 after MI, hematoxylin and eosin (HE) staining (Fig. 3i and Fig. S25) showed that the infarcted myocardial tissues contained cardiomyocytes with disordered, shrunken, and pyknotic nuclei in the ischemic-area, and that some of the cardiomyocytes were replaced by collagenous fibrous tissue. MCN, followed by P and PP, had the greatest protective effect on myocardial remodeling, and PB exerted the least protective effect, consistent with our echocardiography results. These comprehensive effects demonstrated significant therapeutic benefits in a mouse model of MI. To improve the clinical relevance of our study, we further examined the effects of MCN using a mouse model of ischemia-reperfusion (IR) injury. In the IR mode, mice treated with MCN exhibited significant heart function recovery with 64.39 ± 2.799% LVEF MCN (Fig. 3j and Fig. S26). The increase in the recovery of cardiac function was consistent with the findings in our MI model, and HE staining indicated a reduction in the infarcted area (Fig. 3i and Fig. S27). These data reveal that the three constituents of MCN (P, PB, and Ce_xO_y) can operate at the nanoscale, manifesting a tripartite effect, and that this nanomedicine effectively mitigates the shortcomings of traditional antioxidant nanomedicines and demonstrates excellent therapeutic efficacy. Indeed, the therapeutic effect of MCN on MI was much better than that of P, PP, and PB NPs.

MCN-mediated reprogramming of the MIM

The ischemia tissues (at day 3 after MI) treated with or without MCN were collected and RNA was isolated for RNA-seq analysis. The two groups had markedly different mRNA expression profiles, as determined by principal component analysis. There were 457 differentially expressed genes (DEGs) between the MI group and the MCN treatment group, including 256 upregulated mRNAs and 201 downregulated mRNAs (Fig. S28). Based on this difference, Gene Ontology (GO) analysis was performed to determine the biological functions of the proteins encoded by the differentially expressed mRNAs (Fig. 3a). The DEGs between the two groups exhibited enrichment mainly in biological processes, including hypoxia (GO:0001666), ROS metabolism (GO:0072593), apoptosis (GO:2001233), inflammation (GO:0050727), cardiac remodeling (extracellular matrix organization, GO:0030198), and mitochondrial energy metabolism (ATP metabolic process, GO:0046034) (Fig. S29 and Supplementary Tables 6–11). The top eight pathways related to the DEGs were further identified by the Kyoto Encyclopedia of Genes and Genomes (KEGG) enrichment analysis. As shown in Fig. 3b, the DEGs in the MCN treatment group compared to the MI group exhibited enrichment in mitochondrial damage-related pathways, including the apoptosis pathway, hypoxia-inducible factor-1α (HIF-1α) signaling pathway, and p53 signaling pathway. In addition, several genes involved in inflammation-related pathways, such as the tumor necrosis factor (TNF) signaling pathway, mitogen-activated protein kinase (MAPK) signaling pathway, leukocyte transendothelial migration pathway and transforming growth factor-β (TGF-β) signaling pathway, were identified. Gene set enrichment analysis (GSEA) indicated that HIF-1 (NES = 1.77, FDR = 0.0094), p53 (NES = 1.68, FDR = 0.0166), and MAPK (NES = 1.80, FDR = 0.0078) (Figs. S30–S32) were all negatively enriched in the MCN group, suggesting that MCN inhibited the activation of the HIF-1α, p53, and MAPK signaling pathways.

Three key factors—hypoxia, ROS, and H^+—mediate cardiomyocyte death in the MIM through HIF-1, p53, and Bcl-2/adenovirus E1B interacting protein 3 (BNIP3)[24] (Fig. 3c). As shown in Fig. 3d and Fig. S33, the protein levels of the key molecules in infarcted myocardial were consistent with our hypotheses, indicating that MCN significantly reduced p-Histone H2AX (a DNA damage-associated protein), BNIP3 (closely related to pH in the MIM), and P53 (a cell death-related protein that induces pathological progression of MI), compared with those in the sham group. As shown in Fig. 3e, the infarcted myocardial tissues contained an abundance of ROS, and the ROS content was significantly reduced in MCN-treated infarcted myocardial tissues, as measured with a dihydroethidium (DHE) probe. Similarly, MCN treatment greatly reduced the content of ROS in hypoxic primary mouse cardiomyocytes (Fig. S34). This evidence fully proved that MCN effectively eliminated ROS in the MIM. MCN effectively increased the pH in infarcted myocardial tissue, as determined through staining with a pH-specific fluorescent probe (pHrodo)[25]. As an indicator of the O_2 concentration, the expression level of HIF-1α is closely related to the extent of hypoxia in MI[26]. As shown in Fig. 3g and Figs. S35, S36, HIF-1α was significantly upregulated in the infarcted myocardial tissues, and MCN treatment significantly reduced the expression of HIF-1α (Fig. 5g), indicating that MCN had a much stronger ability to relieve MIM hypoxia in the MIM than did P or PP. MCN also increased the concentration of O_2, as determined by evaluation with the $[Ru(dpp)_3]Cl_2$ probe (Fig. S37) in primary cardiomyocytes under hypoxic conditions[27]. The above evidence fully verified that MCN effectively reprogrammed the MIM by decreasing ROS levels, regulating the pH, and generating O_2. Hypoxia is the fundamental cause of the pathological progression of MI. We believe that the ability to convert ROS into O_2 is one of the important mechanisms underlying the potent efficacy of MCN for MI treatment. Overall, O_2 generation and ROS scavenging are both important, and the ability of MCN to accomplish both allows it to effectively treat MI.

MCN protects mitochondrial function and reduces cardiomyocyte apoptosis

The myocardial fluid comprises mainly extracellular tissue fluid and intracellular fluid[28]. In addition to extracellular myocardial tissue fluid, the MIM contains an abundance of cardiomyocytes, macrophages, fibroblasts, and endothelial cells, which contain cellular fluids that determine cell fate[29]. Based on our previous data, MCN was widely distributed in infarcted myocardial tissues, and could alleviate the acidic pH, hypoxia, and high levels of ROS in infarcted myocardial tissues. Moreover, MCN could be efficiently taken up by cardiomyocytes and macrophages under hypoxic conditions. Therefore, we focused on examining the effects of MCN on cardiomyocytes and macrophages, which play a leading role in the pathological progression of MI. Cardiomyocytes possess a notably high mitochondrial density due to their high energy demands[30]. However, the MIM not only promotes the loss of mitochondrial function to generate a ROS burst, but also induces cardiomyocyte death through mitochondrial damage. TEM revealed that MCN accumulated in mitochondria in infarcted myocardial tissues and that these mitochondria still presented a normal morphology despite the presence of MCN (Fig. 4c). However, mitochondrial swelling and rupture and loss of cristae in the inner mitochondrial membrane were observed in the infarcted myocardial tissues without MCN treatment. The colocalization of mitochondria and MCN was investigated in primary cardiomyocytes by

https://doi.org/10.1038/s41467-024-50854-4

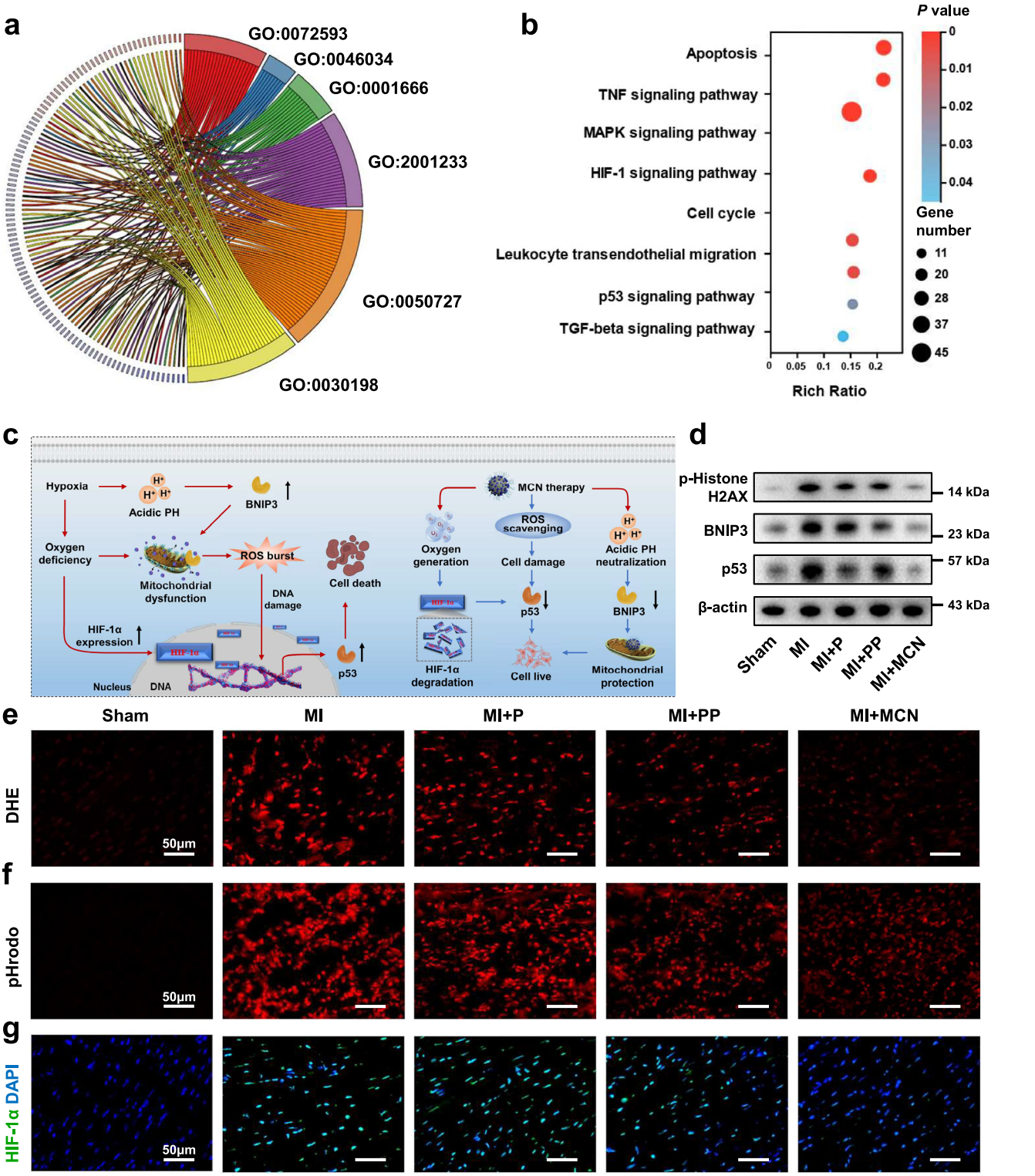

Fig. 3 | RNA-Seq analysis of mice and protective effect of MCN in the hypoxic microenvironment. a Chord diagram showing enriched GO terms of mice with MI treated with or without MCN. **b** Heatmap visualization of the DEGs between the MI NPs group and the MI + MCN group within pathways identified by KEGG enrichment analysis. All data were presented as the mean ± SD. Two-group statistical significance was calculated by unpaired two-tailed Student's *t*-test. **c** Schematic showing that MCN restored the homeostasis of the MIM. **d** Western blot analysis of apoptosis-related proteins (p-Histone H2AX, BNIP3, and p53) in heart tissues from mice subjected to the different treatments on day 1 post-MI. Representative fluorescence images of ROS activity (DHE) (**e**), pH (pHrodo) (**f**), and hypoxia levels (HIF-1α) (**g**) after the different treatments on day 1 post-MI. Scale bar: 50 μm. Replicated across three distinct experiments or $n = 6$ animals per group. Some of the drawing materials for Fig. 3c were downloaded from BioRender.com and are released under a Creative Commons Attribution-NonCommercial-NoDerivs 4.0 International license.

https://doi.org/10.1038/s41467-024-50854-4

Mitotracker and MCN-FITC labeling. As shown in Fig. 4d and Fig. S38, MCN efficiently entered cardiomyocytes and colocalized with red-labeled mitochondria, with a maximum Pearson correlation coefficient for colocalization of 0.67 ± 0.04583. Hypoxia leads to depolarization of the mitochondrial membrane potential in cardiomyocytes, which is the earliest manifestation of oxidative stress damage[31]. As shown in

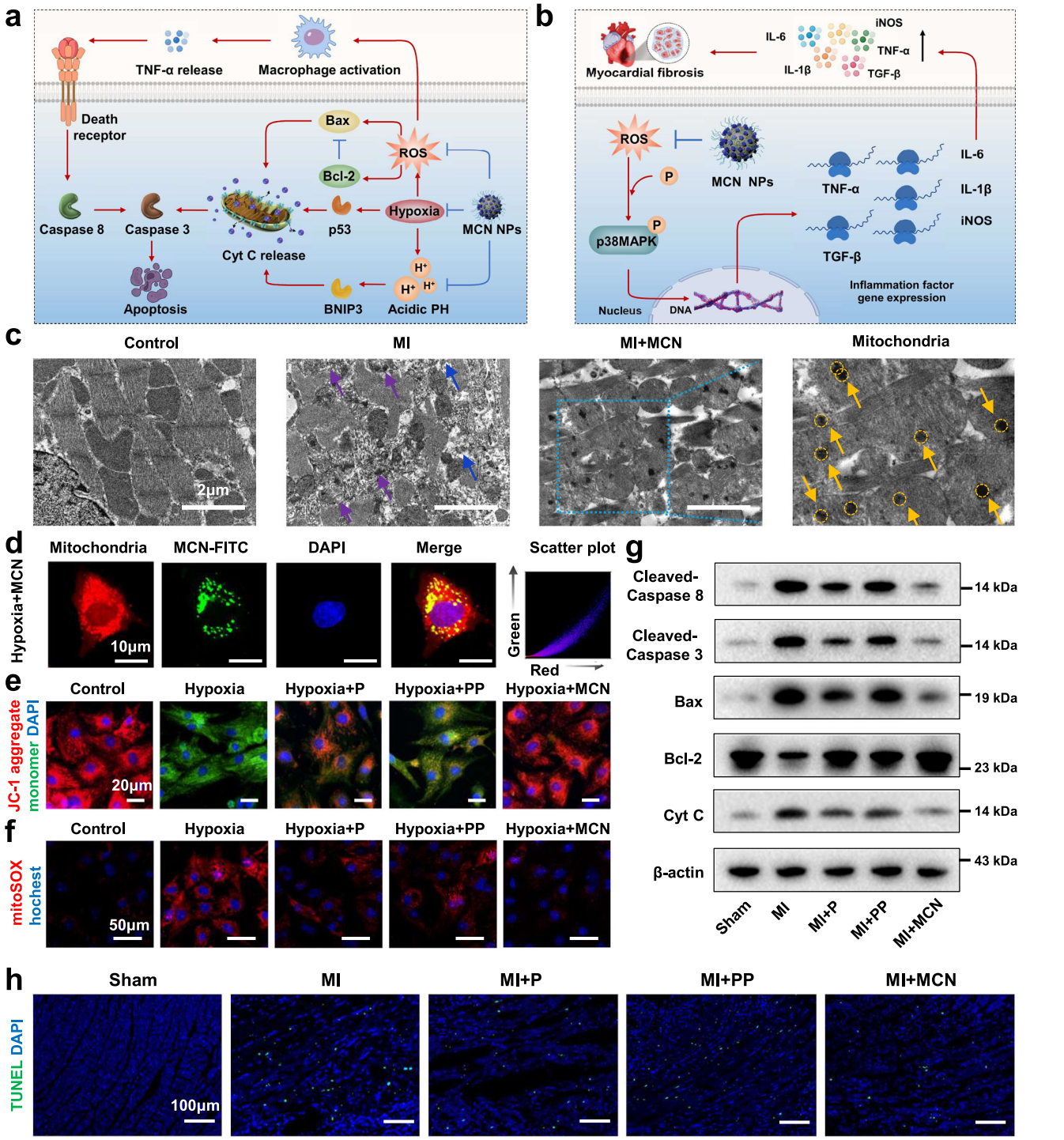

Fig. 4 | Protective effect of MCN on apoptosis via ROS scavenging and O_2 generation. a, **b** Schematic illustration showing that MCN reduced cardiomyocyte apoptosis. **c** Ultrastructural examination of cardiac tissue via TEM reveals the presence of MCN (indicated by yellow arrows) localized on myocardial mitochondria. Scale bar: 2 μm. After MCN treatment, the mitochondria maintain their structural integrity on the right panel, while the middle panel shows notable mitochondrial swelling (highlighted by purple arrows) and fiber dissolution (blue arrows) in the MI group. **d** Representative images and colocalization analysis of MCN-FITC and mitochondria and Pearson coefficient analysis. Scale bar: 10 μm. **e** Variations in mitochondrial membrane potential post-diverse treatments in both normoxic and hypoxic environments are determined using JC-1 staining. Scale bar: 20 μm. **f** The cardiac cells that received P/PP/MCN treatments were tested using mitoSOX staining, which is shown in red. Scale bar: 50 μm. **g** Western blot analysis of apoptosis-related proteins, including cleaved caspase 8, cleaved caspase 3, Bax, Bcl-2, and Cyt C, in the infarct area on day 3 after MI. **h** TUNEL staining of cardiac sections on day 3 after MI and quantitative analysis of the TUNEL results. Scale bar:100 μm. Replicated across three distinct experiments or $n = 6$ animals per group. Some of the drawing materials for Fig. 4a, b were downloaded from BioRender.com and are released under a Creative Commons Attribution-NonCommercial-NoDerivs 4.0 International license.

Fig. 4e and Fig. S39, MCN treatment effectively restored the mitochondrial membrane potential in cardiomyocytes under hypoxic conditions, as determined by staining with the JC-1 probe. Moreover, the effect of MCN was much stronger than that of P or PP. Given its strong mitochondrial targeting ability, MCN efficiently protected mitochondria by eliminating mitochondria-generated ROS, which were detected using a mitochondrial ROS-specific superoxide indicator (MitoSOX)[32]. As shown in Fig. 4f and Fig. S40, the relative fluorescence intensity was 8.469 ± 0.9636 in the hypoxia group, 4.381 ± 0.276 in the P group, 6.178 ± 0.7168 in the PP group, and 2.341 ± 0.197 in the MCN group. The mitochondrial DNA copy number (mtDNA)[33], an index of the mitochondrial genome count, is also a sensitive indicator of mitochondrial function. The mtDNA copy number in the hypoxia group was only 10.56% of that in the control group, while the mtDNA copy number in the MCN group was 63.006% of that in the control group (Fig. S41). MCN also effectively reversed the hypoxia-induced reduction in ATP production (Fig. S42). The above experimental evidence and transcriptomic data revealed that MCN effectively protected mitochondria against ROS-mediated damage, and significantly restored mitochondrial function.

Damage to mitochondria can directly induce apoptosis in cardiomyocytes[34]. Apoptosis is mediated through two main pathways: the intrinsic (mitochondrial) pathway and the extrinsic (inflammatory) pathway (Fig. 4a, b)[30]. We hypothesized that MCN could decrease the occurrence of cardiomyocyte apoptosis by reducing the activation of both the mitochondrial and inflammatory apoptotic pathways. The protein levels of cleaved caspase 8, cleaved caspase 3, Bax, and cytosolic cyt C were much greater in the MI group than in the sham group, and the expression level of the antiapoptotic protein Bcl-2 was decreased. However, MCN treatment significantly reversed these effects (Fig. 4g and Fig. S43). As shown in Fig. 4h and Fig. S44, the MI group exhibited a high apoptosis rate (47.21 ± 2.568%), according to the TdT-mediated dUTP nick end labeling (TUNEL) assay, while the MCN group exhibited the lowest apoptosis rate (22.57 ± 5.835%). The MCN group also showed a significantly reduced infarct area of 29.07 ± 3.584% with TTC staining at day 3, as determined by 2,3,5-triphenyltetrazolium (TTC) staining, indicating the effectiveness of MCN in reducing the infarct area (Fig. S45). These findings suggested that both the intrinsic and extrinsic apoptotic pathways were inhibited by MCN via its protective effects on mitochondria protection and inhibitory effects on apoptotic proteins.

MCN reduces inflammation and fibrosis

Disruption of the MIM leads to a massive and rapid increase in the production of ROS, which not only directly damage cardiomyocytes but also trigger the production of damage-associated molecular patterns (DAMPs)[35]. These DAMPs further cause a shift in the polarization of the recruited macrophages towards the M1 phenotype, thus increasing the release of proinflammatory cytokines and fibroblast growth factors and eventually leading to myocardial fibrosis[36]. First, primary mouse bone marrow-derived macrophages (BMDMs) were extracted, and the differentiation of BMDMs into M1 macrophages was then induced by treatment with lipopolysaccharide. Notably, M1 macrophages produced an abundance of ROS after polarization towards the M1 phenotype, and MCN effectively reduced the ROS content in these M1 macrophages because of its excellent ability to scavenge ROS (Fig. S46). Consistent with our hypothesis, MCN significantly promoted M2 macrophage polarization, and this effect was significantly greater than that in the PP and P groups (Fig. S47). We observed similar effects of MCN in infarcted myocardial tissue. As shown in Fig. 5a, b, after MCN treatment, a significantly increased number of $CD206^+$ cells (M2 macrophages) cells were detected in the infarcted myocardial tissues. Moreover, the effect of MCN was far better than that of either P NPs or PP NPs. Moreover, the mRNA expression of *IL-6*, *IL-1β*, *iNOS*, and *TNF-α* was significantly decreased in infarcted myocardial tissues after MCN treatment, as determined by qPCR (Fig. 5c–f). We observed consistent effects in BMDMs (Fig. S48). In addition, MCN treatment reduced the phosphorylation of p38 MAPK (Fig. 5g–j), suggesting that the reduction in inflammation was related to the inhibition of the p38 MAPK signaling pathway[37]. Myocardial fibrosis is key to myocardial remodeling after MI and is strongly associated with poor prognosis[38]. TGF-β is involved in the progression of fibrosis after MI and directly affects p38 MAPK phosphorylation[39]. As shown in Fig. 5g, i, the expression of TGF-β was decreased in the infarcted myocardial tissues after MCN treatment. MI hearts were larger in size, had a thinner ventricle wall, and exhibited collagen deposition in the left ventricle, as indicated by Masson staining (blue), suggesting the presence of severe fibrosis in the left ventricle (the fibrotic area accounted for 33.85 ± 1.343% of the total area) (Fig. 5k). In strong contrast, in the MCN group, the degree of cardiac fibrosis was decreased (17.28 ± 1.463%) (Fig. 5l) and the thickness of the left ventricle was significantly increased (Fig. 5m). Notably, the area of myocardial fibrosis was greater in the PP group (30.08 ± 1.506%) compared than that in the P group (24.98 ± 1.172%) (Fig. 5l) because the toxic ·OH produced by the PB in PP NPs may aggravate myocardial fibrosis in infarcted myocardial tissues. Sirius red staining was also used to evaluate cardiac fibrosis and collagen deposition, and the lowest degree of left ventricular fibrosis was observed after MCN treatment (Fig. S49). The above evidence indicated that MCN reduced myocardial fibrosis by inhibiting the p38 MAPK and TGF-β signaling pathways.

Biocompatibility of MCN

MCN is composed of P, PB, PEG, and Ce_xO_y. Among these components, P is the main component of human melanin, and its biocompatibility has been fully verified[40]. PB and PEG are an FDA-approved drug and excipients, respectively, and their biological safety has also been carefully determined. To date, Ce_xO_y-based nanomedicines have been widely used to treat different diseases and can maintain excellent biocompatibility at specific doses[41]. Notably, the content of Ce in MCN (only 0.08%) is much lower than that in previous Ce_xO_y nanomedicines[42]. Therefore, MCN should exhibit excellent biocompatibility. Under normoxic conditions, MCN did not affect the viability of cardiomyocytes even at ultrahigh concentrations (40 μg/mL). In comparison, the viability of cardiomyocytes was significantly improved under hypoxic conditions upon treatment with 1 μg/mL MCN (Fig. S50 a, b). The in vivo toxicity of MCN was further evaluated by assessment of the hemolysis rate, routine blood examination, liver and kidney function tests, and HE staining. MCN did not cause hemolysis even at high concentrations (Fig. S51). The blood routine test results (Fig. S52) and liver and kidney function were normal in the MCN-treated mice compared with the control mice (Fig. S53). The morphology of the lungs, liver, spleen, and kidneys was normal in the MCN-treated mice, as determined by HE staining (Fig. S54). The above results indicated that MCN exhibited favorable biological safety, providing a basis for its further clinical application.

Methods

Experimental animals

Male C57BL/6J mice (8–12 weeks, 20–25 g) were purchased from the Animal Center of Central South University. All animal studies were performed in accordance with guidelines and protocols approved by the Ethics Committee of Xiangya Hospital (No. 2022020390). The animals were maintained under standard laboratory conditions: 25 ± 1 °C, 50% relative humidity, and a 12 h/12 h dark/light cycle, with free access to food and water.

Synthesis of P NPs

Dopamine hydrochloride (0.75 g) was dissolved in 10 mL water, followed by the sequential addition of 50 mL ethanol, 110 mL deionized water, and 3 mL ammonia. The mixture was heated to 30 °C and stirred

https://doi.org/10.1038/s41467-024-50854-4

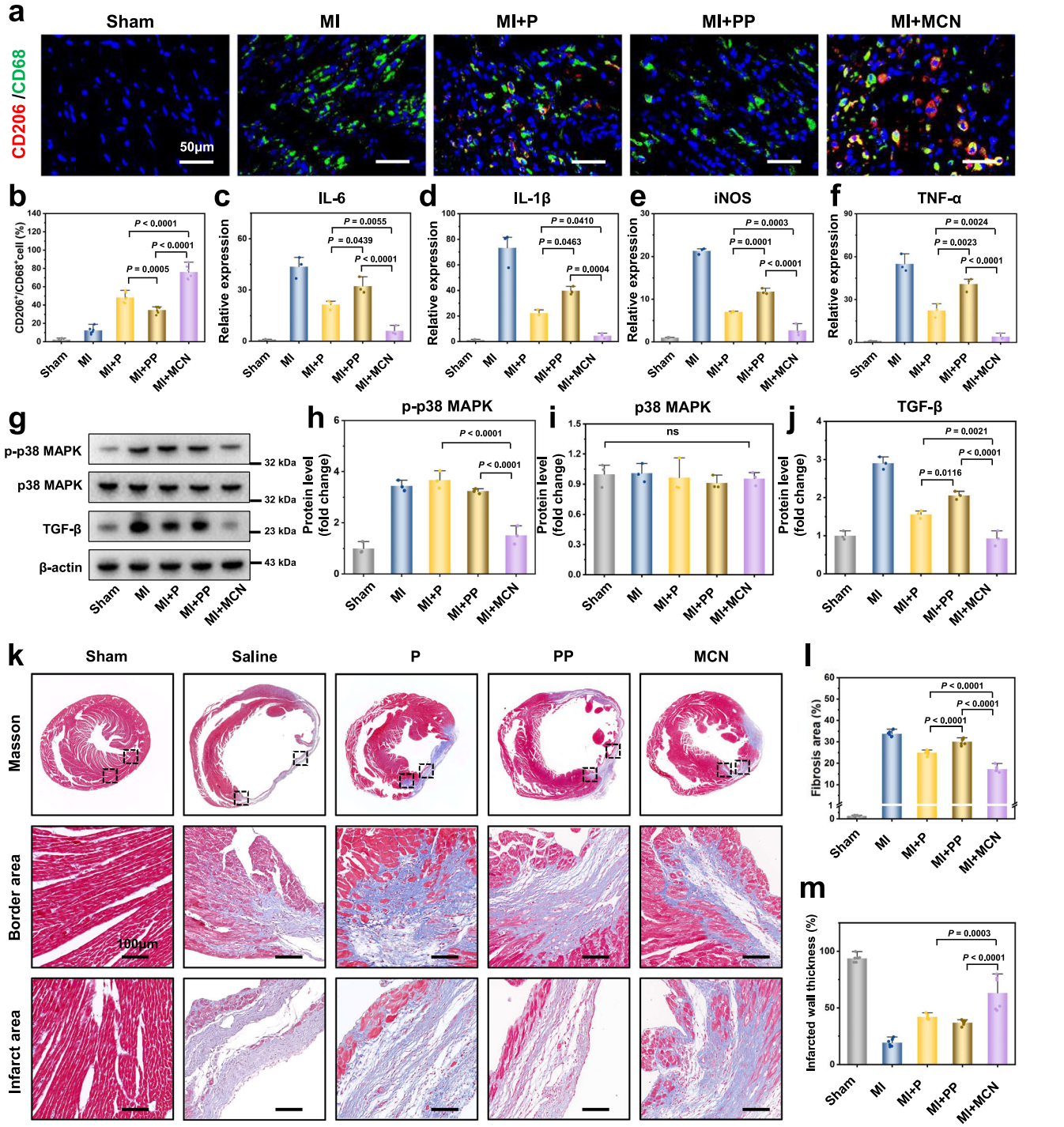

Fig. 5 | Effect of MCN on inflammation in the myocardial cells of MI mice. **a** Representative images of heart CD68 (macrophage marker, green) and CD206 (M2 macrophage marker, red) immunostaining on day 3 after MI. Scale bar: 50 μm. **b** Quantitation analysis of the $CD206^+/CD68^+$ cells. **c**–**f** RT–PCR of proinflammatory markers: *IL6*, *IL1β*, *TNFα*, and *iNOS* on day 3 after MI. **g** Western blot of TGF-β signaling pathway protein levels of TGF-β, p-p38 MAPK, and p38 MAPK in the infarct area on day 3 after MI. Quantitative analyses of protein levels: p-p38 MAPK (**h**), p38 MAPK (**i**), and TGF-β (**j**). **k** Representative images of Masson's staining on day 28 after MI. Scar bar:100 μm. Quantitation analysis of the fibrotic region (**l**) and thickness of the infarcted wall (**m**). Replicated across three distinct experiments or $n = 6$ animals per group. All data were presented as mean ± SD. Two-group statistical significance was calculated by unpaired two-tailed Student's *t*-test, and three-or-more-group statistical significance was calculated by one-way ANOVA followed by Bonferroni post hoc correction.

for 24 h. Post reaction, the product was centrifuged at 1355 × *g* for 10 min, washed 8–10 times, and P NPs was obtained.

Synthesis of PP NPs

P NPs (40 mg) were dissolved in 50 mL of deionized water, forming solution A. Separately, $FeCl_3$ (50 mg) and $K_3Fe[CN]_6$ (57.69 mg) were dissolved in 10 mL of deionized water, creating solution B. Then, 1 mL of solution B was diluted with 49 mL water and gradually added to solution A over 30 min using a micro syringe pump at 25 °C. The mixture was stirred for 6 h, centrifuged at 1355 × *g* for 10 min, washed five to eight times, and PP NPs was obtained.

Synthesis of MCN

PP NPs (30 mg) and $Ce(NO_3)_3$ (0.174 g) were dissolved into 50 mL of deionized water and stirred at 25 °C for 15 min. Then, 1 mL of 0.12 M hydrochloric acid was added to the mixture and reacted at 95 °C for 10 min, and defined as solution C. After cooling, the solution C was washed three to five times (1355 × *g*/10 min) to remove the precipitate. Solution C (10 mg) and NH_2-PEG-NH_2 (12.5 mg) were dissolved in 10 mL of pH 8.5 tris solution at 25 °C for 24 h. Washing three to five times (1355 × *g*/10 min) and MCN was obtained.

Synthesis of MCN-FITC NPs

First, MCN (10 mg) was added to 8 mL of deionized water, and FITC (2 mg) was dissolved into 2 mL of DMSO. Then, the two mixtures were reacted at 25 °C for 6 h in the dark to obtain FITC-MCN. Finally, FITC-MCN was purified after dialysis for 24 h.

Synthesis of PB NPs

About 20 mL 0.1 mmol $K_4[Fe(CN)_6]$ aqueous solution was slowly added into 80 mL mixed solution containing 0.1 mmol $FeCl_3$ and 10 mmol PVP within 30 min with a micro-scale injection pump, and was vigorously stirred at 60 °C for 6 h. After washing five to eight times (1355 × *g*/10 min), PB NPs was obtained.

Characterization

The structures of the nanoparticles were observed by a TECNAI G2 high-resolution transmission electron microscope. XPS was measured by a VG ESCALAB MKII spectrometer. XPSPEAK software (version 4.1) was used to deconvolute the narrow-scan XPS spectra of the C1*s*, N1*s*, O1*s*, Fe2*p*, and Ce3*d* of MCN. Fourier transform infrared (FTIR) spectroscopy was recorded by a Bruker Vertex 70 spectrometer (2 cm^{-1}). The ultraviolet-visible (UV-vis) spectra were acquired by a VARIAN CARY 50 UV/Vis spectrophotometer. Inductively coupled plasma–mass spectrometry (ICP–MS) was measured by a thermo/Jarrell ash advantage atomscan inductively coupled argon plasma spectrometer.

Superoxide anion scavenging assay

In vitro. $O_2^{\bullet-}$ scavenging ability was analyzed by the tetrazolium blue (NBT) method[40]. Briefly, 390 μL methionine, 6 μL riboflavin, 22.5 μL NBT, 1.5 mL PBS (pH 7.4), and different concentrations of P/PP/MCN (0, 2.5, 5, 10, and 20 μg/mL) were added, and fully dissolved in 3 mL water. The cuvette was exposed to UV light, and 5 min later, the absorbance was detected at 560 nm. Then the inhibition of NBT photochemical reduction was used to determine the $O_2^{\bullet-}$ scavenging abilities.

Hydroxyl radical generation

The typical TMB method was used to detect the ·OH. Briefly, 2910 μl PBS (0.01 M, pH 4/pH 6.5/pH 7.4) and P/PP/MCN (10 μL, 5.5 mg/mL), 30 μL TMB (25 mM), and 60 μL H_2O_2 (0.1 M) were sequentially added into the Eppendorf tube and mixed. After being reacted for 10 min, the absorbance changes of the TMB oxidized form at λ_{max} = 652 nm (ε = 39,000 $M^{-1}{\cdot}cm^{-1}$) were recorded, and the ·OH content was calculated through TMB catalyzes oxidation reactions.

$ONOO^-$ scavenging assessment

Pyrogallol red was used to detect the scavenging ability of $ONOO^-$[43]. Pyrogallol red has a specific absorption peak at 540 nm, and $ONOO^-$ can quench pyrogallol red and reduce its specific absorption peak. Briefly, 10 μL pyrogallol red (5 mM), 9 μL $ONOO^-$(1.73 mM), and MCN with different concentrations (0, 2.5, 5, and 10 μg/mL) or P/PP (10 μg/mL) were mixed. The pyrogallol red solution and pyrogallol red containing $ONOO^-$ were set as control. After being reacted for 15 min, the absorbance of pyrogallol red at 540 nm was recorded by UV-vis spectrophotometry, and the $ONOO^-$ scavenging ability was calculated.

O_2 generation assay

H_2O_2 (1.2 M H_2O_2) and P/PP/MCN (3 mg) were mixed, and PBS (pH 4/pH 6.5/pH 7.4) was added to 50 mL in an oxygen-free environment. The O_2 concentration was measured by a dissolved oxygen meter (SMART SENSOR, AR8406) for 30 min. The O_2 bubbles were observed in an Eppendorf tube. H_2O_2 (1.2 M) and 240 μg of P/PP/MCN were mixed in 4 mL of PBS in an oxygen-free environment, and O_2 bubbles were recorded in different groups.

MI model

Under approval from the Medical Ethics Committee of Xiangya Hospital, Centre South University, male C57BL/6J mice (8–12 weeks, 20–25 g) were anesthetized with isoflurane[12]. After intubation and ventilation, a 1 cm incision was made between the left third and fourth intercostal spaces to expose the heart. The left anterior descending artery (LAD) was ligated 2 mm below the left auricle by using a 10-0 suture needle with thread. Sham animals underwent similar procedures minus the LAD ligation. Post-operatively, buprenorphine (0.1 mg/kg) and cefazolin (100 mg/kg) were administered twice daily for 2 days.

Echocardiography

After anesthesia with isoflurane, mice were positioned on a heated platform. Echocardiographic assessments of left ventricular function using a 20 MHz sensor (ZS3 Exp, Mindray, Nanjing, China) were conducted on days 1, 3, 7, 14, and 28 post-surgeries. Parameters including LVEF, LVFS, EDV, ESV, LVIDd, and LVIDs were determined from M-Mode echocardiography. Ventricular diameter (D) was noted, and LVEDV and LVESV were calculated using $Vol = 7.0 \times D^3/(2.4 + D)$.LVEF was computed as $LVEF(\%) = (LVEDV - LVESV)/LVEDV \times 100\%$. LVIDd and LVIDs represented ventricular diameters at diastole and systole ends, respectively. LVFS was derived as $LVFS(\%) = (LVIDd - LVIDs)/LVIDd \times 100\%$. All data analyses were conducted by a blinded investigator to treatment groups.

HE staining, Masson staining, and Sirius red staining

Animal organs were collected on day 28 after surgery and fixed with 4% PFA for 24 h. After dehydration, the samples were embedded into paraffin blocks and cut into 4-μm sections. Place the sections sequentially in xylene, ethanol, and distilled water for hydrated. For HE staining, the sections were stained in Harris hematoxylin for 3 min, washed with tap water, differentiated with 1% hydrochloric acid alcohol for a few seconds, rinsed with tap water, blue in 0.6% ammonia water, and rinsed with running water. Then stain the sections in eosin solution for 1 min for staining of cytoplasm. After that, the sections were sequentially placed in ethanol and xylene to dehydrate and mounted with neutral resin. Additionally, the sections were stained with a Masson's trichrome stain kit (Servicebio, G1006). Briefly, the sections were sequentially treated with potassium dichromate overnight and stained with iron hematoxylin, picric acid fuchsin, phosphomolybdic acid, and aniline blue, followed by dehydration and mounting. For Sirius red staining, staining was performed using Sirius red dye after hydration, followed by dehydration and mounting. After staining, the sections were observed and imaged under a light microscope (Leica DM3000 LED).

TEM

Myocardial tissues harvested at day 1 post-surgery, were cut into blocks <1 mm^3. These were fixed in a TEM fixation solution for 2 h and subsequently in a 1% osmium acid mixture for 2–3 h. Following gradient dehydration, tissues were embedded and solidified. Sections of 60–80 nm thickness were prepared using an ultratome and double-stained with 3% uranyl acetate-lead citrate. Imaging was performed with a Jeol 1200EX transmission electron microscope.

ROS scavenging assessment

The DHE staining of tissue used a Frozen section ROS detection kit (BioRab Technology, China, HR9069). Freshly harvested hearts (within 2 h after section) were harvested on day 1 post-MI surgery. Add 200 μL of wash solution to cover the entire surface of the section and let it sit for 3–5 min at room temperature. Carefully remove the wash solution, add 200 μL of staining solution (1:1000), and incubate in a 37 °C incubator in the dark for 30 min. These sections were stained with DHE as per the manufacturer's instructions and visualized under a Zeiss LSM900 confocal microscope (Germany). For each section, a minimum of three random imaging fields within the infarcted area were chosen for fluorescence intensity quantification using ImageJ.

Cardiomyocyte ROS levels were determined using the DHE assay kit (Beyotime, S0063). To further measure intracellular ROS levels, Cardiomyocytes were seeded at 1×10^5/well in a 6-cm dish and cultured for 12 h. Post incubation with P, PP, or MCN under hypoxia for 12 h, cells were stained with a 5 μM DHE assay kit (Beyotime, S0063) for 30 min at 37 °C in the dark. The cells were washed three times with PBS and analyzed by flow cytometry (Cytek, DxpAthena, 01-DXPSF13-01).

Fluorogenic pH sensing of mouse MI area

To measure pH in the ischemic region, pHrodo Red (Thermo Fisher, P35372) was utilized. Freshly harvested hearts, 1 day post-surgery, were incubated with pHrodo Red (1:500) for 5 h at 37 °C. After incubation, the samples were embedded in OCT and quickly frozen-sectioned. Fluorescence from pHrodo Red was directly visualized using a Zeiss LSM900 confocal microscope (Germany). For each section, fluorescence intensity from at least three randomly selected imaging fields within the infarcted area was quantified using ImageJ.

TTC staining

On the fourth day after MI surgery, hearts were harvested, frozen at −20 °C for an hour, the heart was sectioned, and incubated with 1% TTC solution (Sigma, T8877) at 37 °C for 15 min in darkness. Post-staining, sections were fixed in 4% PFA, and images were captured using a light Leica M205 microscope (Germany).

TUNEL staining

Apoptosis was assessed using the TUNEL assay kit (Beyotime Biotechnology, C1088). Fresh frozen heart sections, 3 days post-surgery, were fixed cells with 4% paraformaldehyde for 60 min. The sections were washed with PBS two times, then PBS with 0.5% Triton X-100 was added and incubated at room temperature for 5 min. TUNEL detection solution was prepared as per the manufacturer's instructions. Add 100 μL of TUNEL detection solution to the sample and incubate at 37 °C away from light for 60 min. Wash with PBS three times and subsequently stain with DAPI. Images were captured using a Zeiss LSM900 confocal microscope (Germany).

Immunofluorescence staining

Evaluation of HIF-1α staining was carried out on hearts harvested 1 day post-surgery. CD68 and CD206 staining were performed on hearts harvested 3 days post-surgery. Post fixation, dehydration, and clearing, heart sections of 4-μm thickness were prepared. The sections underwent rehydration in increasing ethanol concentrations, citrate buffer exposure for 10 min at microwave high temperature, 0.5% Triton X-100 permeabilization for 10 min, and blocking in 5% goat serum for 30 min. These sections were incubated overnight at 4 °C with primary antibodies (detailed in Supplementary Table 1). Following PBS washes, sections were incubated with secondary antibodies (Supplementary Table 1) for an hour at room temperature, protected from light. DAPI was used for nuclei counterstaining, and visualization was done using a Zeiss LSM900 confocal microscope (Germany).

Protein extraction and western blot

Samples were lysed using RIPA buffer (Beyotime, China) and centrifuged at 1623 × *g* for 15 min at 4 °C. Protein concentration was determined using the BCA kit (Beyotime, China). Following SDS-PAGE, proteins were transferred to membranes which were subsequently blocked. Membranes were then incubated with primary antibodies (Supplementary Table 2), followed by the appropriate secondary antibodies (Supplementary Table 2). Visualization was achieved using a chemiluminescent imaging system (Bio-Rad), and band intensities were quantified using ImageJ software.

RNA isolation and quantitative real-time PCR

Total RNA was isolated by Trizol method. cDNA was synthesized by PrimeScript RT Reagent Kit (Takara, Japan). qPCR reaction was performed using TB Green Premix Ex Taq (Takara, Japan). The results were calculated and normalized to GAPDH by the $2^{-\Delta\Delta Ct}$ method.

Neonatal cardiomyocyte isolation and culture

Neonatal cardiomyocytes are isolated from hearts using the Miltenyi Neonatal Heart Dissociation Kit (130-098-373)[44]. After harvesting hearts from postnatal day 1 C57BL/6J pup and washing with PBS twice, the hearts are enzymatically digested and dissociated with the gentleMACS dissociator. The cell mixture is filtered through a 70-μm strainer, centrifuged at 600 × *g* for 5 min, and the resulting cardiomyocytes are resuspended in high-glucose DMEM supplemented with 10% FBS for culture.

BMDMs isolation and culture

To isolate BMDMs from C57BL/6J mice (8–12 weeks old, male), the mice are euthanized, and the hind limbs are harvested[45]. The femurs are exposed by removing muscle tissue, both ends are snipped, and bone marrow is flushed into DMEM with 10% FBS using a syringe. After centrifugation (300 × *g*, 5 min), the cells are cultured in DMEM with 10% FBS, 1% penicillin/streptomycin, and 20 ng/mL M-CSF for 7 days. Post-differentiation, BMDMs are ready for further experiments.

Cell viability assay

The cell proliferation was evaluated with a Cell Counting Kit-8 (CCK-8, Dojindo, Kumamoto, Japan) by following the manufacturer's instructions. Briefly, cardiomyocytes were seeded in 96-well plates (1×10^4/well) and cultured overnight in high-glucose DMEM with 10% FBS. Following normoxia (21% O_2, 5% CO_2, 37 °C), they were treated under hypoxia (1% O_2, 5% CO_2, 94% N_2, 37 °C) with PBS or NPs for 12 h. Cells were incubated with CCK-8 reagent (10:1) for 4 h at 37 °C post-treatment. Absorbance was then assessed using a BioTek plate reader.

O_2 probe detection

Cardiomyocytes, seeded at 3×10^4/well on coverslips in 24-well plates, were cultured overnight. Post incubation with MCN for 12 h under 1% oxygen, and they were washed with PBS one time. $[Ru(dpp)_3]Cl_2$ probe (Bestbio, China, BB-48216) was used to determine the intracellular oxygen content. Use a complete medium to dilute $[Ru(dpp)_3]Cl_2$ probe (1:100) and incubate cells for 60 min at 37 °C. Wash with medium three times. Stain with Hoechst for 10 min and capture fluorescent images using a Zeiss LSM900 confocal microscope (Germany).

Subcellular localization

The subcellular localization of MCN was imaged by the confocal microscopy. Cardiomyocytes, seeded at 3×10^4/well on coverslips in 24-well plates, were cultured overnight and then treated with MCN-FITC for 2 h. Cells were stained with MitoTracker Red (Beyotime, China, C1049B) for 30 min and Hoechst for 10 min, both at 37 °C. The images were acquired with a confocal laser scanning microscope (Zeiss, LSM900, Germany) and analyzed by ImageJ software (NIH, MD, USA).

Intracellular mitochondrial superoxide (mitoSOX) levels measurement

To further measure intracellular mitoSOX level, Cardiomyocytes were seeded at 1×10^5/well in a 6-cm dish and cultured for 12 h. Post incubation with P, PP, or MCN under hypoxia for 12 h, cells were stained with 5 μM mitoSOX (M36008, Thermo Fisher Scientific) for 10 min at 37 °C in the dark. Then, cells were stained with Hoechst for 10 min. After washing with PBS two times, cell round coverslips were visualized under a Zeiss LSM900 confocal microscope (Germany). For each round coverslip, a minimum of three random imaging fields within the infarcted area were chosen for fluorescence intensity quantification using ImageJ.

Mitochondrial membrane potential measurement

Mitochondrial membrane potential was measured by the assay kit with JC-1 (Beyotime, China, C2005). Cardiomyocytes cultured on coverslips in 24-well plates with a density of 3×10^4/well were incubated with P, PP, or MCN, respectively, and cultured with DMEM under hypoxia conditions (1% O_2) for 12 h. Post incubation with P, PP, or MCN under hypoxia for 12 h, cell round coverslips were washed with PBS one time. JC-1 working solution was prepared as per the manufacturer's instructions. Add 0.5 mL JC-1 working solution and incubate for 20 min at 37 °C in the dark. Then, cell round coverslips were washed with staining buffer (1:5) two times. Stain with Hoechst for 10 min and wash with PBS three times. The images were acquired with a confocal laser scanning microscope (Zeiss, LSM900, Germany) and analyzed by ImageJ software (NIH, MD, USA). The ratio of red and green fluorescent intensities indicated changes in the mitochondrial membrane potential.

Detection of ATP generation

The ATP detection kit (Beyotime, China, S0027) was used to detect ATP generation. Cardiomyocytes were seeded in 96-well plates (1×10^4/well) and cultured overnight in high-glucose DMEM with 10% FBS. Post incubation under normoxia or with P, PP, or MCN under hypoxia for 12 h, cells were lysed with 200 μL lysis solution and centrifuged at 12,000 × *g* for 5 min at 4 °C. The supernatant was mixed with 100 μL ATP detection working solution by following the manufacturer's instructions. The concentration of ATP was measured with a plate reader (Luminometer, BioTek, America).

Mitochondrial DNA copy number

MtDNA copy number was quantified using quantitative real-time PCR. DNeasy Blood and Tissue Kit (Qiagen, Hilten, Germany, 69504) was used to extract DNA from the cells. Mitochondrially encoded Cytochrome C Oxidase II (MT-CO_2) and β-actin (ACTB) were quantified with the primers, respectively. The quantitative real-time PCR was undertaken by following the manufacturer's manuals. The results were calculated with ΔΔCt value and normalized to ACTB.

Hemolysis assay

Under anesthesia, animal blood was drawn from the retro-orbital plexus, mixed with 5 mL PBS, and centrifuged at 1008 × *g*. The supernatant was removed, and the erythrocytes were diluted to 2% using PBS. MCN were prepared at concentrations of 1, 5, 25, 125, 500, 1000, and 2000 μg/mL in PBS. These were mixed with the 2% erythrocyte solution, incubated, then centrifuged. The OD of the supernatant was measured at 570 nm.

Bulk RNA sequencing

Three days post-MI surgery, the ischemic regions of dissected hearts were isolated. RNA was extracted via the Trizol method. Libraries were sequenced on the BGI platform. Raw data were aligned to the mm10 mouse genome using Bowtie2.

Analysis of DEGs

After data normalization using the "limma" R package, PCA was done with "factoextra". DEGs were identified based on log2 (Fold Change) ≥1 and $P < 0.05$. "ggplot2" generated the volcano and heatmap plots, while significant genes were visualized with "ComplexHeatmap".

Statistical analysis

All data were presented as the mean ± SD. Comparisons between two groups were performed with an unpaired two-tailed Student's *t*-test. Multiple comparisons were performed by using one-way ANOVA. Statistical significance was considered when $P < 0.05$.

Reporting summary

Further information on research design is available in the Nature Portfolio Reporting Summary linked to this article.

Data availability

Data supporting the findings of this study are available in the article, its Supplementary information, the source data file and from the corresponding author upon request. Bulk RNA-sequencing data can be accessed from SRA website [https://www.ncbi.nlm.nih.gov/sra/] with the accession number: SRR29489947, SRR29489948, SRR29489949, SRR29489950, SRR29489951, SRR29489952, SRR29489953, SRR29489954, and SRR29489955. Source data are provided with this paper.

References

1. Zhang, Q. et al. Signaling pathways and targeted therapy for myocardial infarction. *Signal Transduct. Target Ther.* **7**, 78 (2022).
2. Roth, G. A. et al. Global burden of cardiovascular diseases and risk factors, 1990-2019: update from the GBD 2019 study. *J. Am. Coll. Cardiol.* **76**, 2982–3021 (2020).
3. Garlapati, V. et al. Targeting myeloid cell coagulation signaling blocks MAP kinase/TGF-beta1-driven fibrotic remodeling in ischemic heart failure. *J. Clin. Invest.* **133**, e156436 (2023).
4. Shilo, M. et al. Injectable nanocomposite implants reduce ROS accumulation and improve heart function after infarction. *Adv. Sci.* **8**, e2102919 (2021).
5. Davidson, S. M. et al. Progress in cardiac research: from rebooting cardiac regeneration to a complete cell atlas of the heart. *Cardiovasc. Res.* **117**, 2161–2174 (2021).
6. Weissman, D. & Maack, C. Mitochondrial function in macrophages controls cardiac repair after myocardial infarction. *J. Clin. Invest.* **133**, e167079 (2023).
7. Li, X. et al. Ischemic microenvironment-responsive therapeutics for cardiovascular diseases. *Adv. Mater.* **33**, e2105348 (2021).
8. Wilson, A. D. et al. Acidic environments trigger intracellular H +–sensing FAK proteins to re-balance sarcolemmal acid-base transporters and auto-regulate cardiomyocyte pH. *Cardiovasc. Res.* **118**, 2946–2959 (2022).
9. Redd, M. A. et al. Therapeutic inhibition of acid-sensing ion channel 1a recovers heart function after ischemia-reperfusion injury. *Circulation* **144**, 947–960 (2021).
10. Long, X. et al. Revitalizing ancient mitochondria with nano-strategies: mitochondria-remedying nanodrugs concentrate on disease control. *Adv. Mater.* **36**, e2308239 (2024).
11. Guan, Y. et al. Rescuing cardiac cells and improving cardiac function by targeted delivery of oxygen-releasing nanoparticles after or even before acute myocardial infarction. *ACS Nano* **16**, 19551–19566 (2022).
12. Sun, Q. et al. A self-sustaining antioxidant strategy for effective treatment of myocardial infarction. *Adv. Sci.* **10**, e2204999 (2023).

13. Wang, Y. et al. Advancements of Prussian blue-based nanoplatforms in biomedical fields: progress and perspectives. *J. Control Release* **351**, 752–778 (2022).
14. Kim, Y. G. et al. Ceria-based therapeutic antioxidants for biomedical applications. *Adv. Mater.* **36**, e2210819 (2024).
15. Liu, Y. et al. Comprehensive insights into the multi-antioxidative mechanisms of melanin nanoparticles and their application to protect brain from injury in ischemic stroke. *J. Am. Chem. Soc.* **139**, 856–862 (2017).
16. Zhou, T. et al. Prussian blue nanoparticles stabilize SOD1 from ubiquitination-proteasome degradation to rescue intervertebral disc degeneration. *Adv. Sci.* **9**, e2105466 (2022).
17. Estelrich, J. & Busquets, M. A. Prussian blue: a nanozyme with versatile catalytic properties. *Int. J. Mol. Sci.* **22**, 5993 (2021).
18. Wang, X. et al. Tumor-targeted disruption of lactate transport with reactivity-reversible nanocatalysts to amplify oxidative damage. *Small* **17**, e2100130 (2021).
19. Kim, J. et al. Synergistic oxygen generation and reactive oxygen species scavenging by manganese ferrite/ceria co-decorated nanoparticles for rheumatoid arthritis treatment. *ACS Nano* **13**, 3206–3217 (2019).
20. Piacenza, L., Zeida, A., Trujillo, M. & Radi, R. The superoxide radical switch in the biology of nitric oxide and peroxynitrite. *Physiol. Rev.* **102**, 1881–1906 (2022).
21. Taiariol, L., Chaix, C., Farre, C. & Moreau, E. Click and bioorthogonal chemistry: the future of active targeting of nanoparticles for nanomedicines? *Chem. Rev.* **122**, 340–384 (2022).
22. Triposkiadis, F. et al. The continuous heart failure spectrum: moving beyond an ejection fraction classification. *Eur. Heart J.* **40**, 2155–2163 (2019).
23. Wang, M. et al. Precisely inhibiting excessive intestinal epithelial cell apoptosis to efficiently treat inflammatory bowel disease with oral pifithrin-alpha embedded nanomedicine (OPEN). *Adv. Mater.* **35**, e2309370 (2023).
24. Madhu, V. et al. The mitophagy receptor BNIP3 is critical for the regulation of metabolic homeostasis and mitochondrial function in the nucleus pulposus cells of the intervertebral disc. *Autophagy* **19**, 1821–1843 (2023).
25. Liu, C. L. et al. Reduced Nhe1 (Na(+)-H(+) exchanger-1) function protects ApoE-deficient mice from Ang II (Angiotensin II)-induced abdominal aortic aneurysms. *Hypertension* **76**, 87–100 (2020).
26. Kimura, W. et al. Hypoxia fate mapping identifies cycling cardiomyocytes in the adult heart. *Nature* **523**, 226–230 (2015).
27. Zhou, P. W. et al. 320-fold luminescence enhancement of [Ru(dpp)] Cl dispersed on PMMA opal photonic crystals and highly improved oxygen sensing performance. *Light Sci. Appl.* **3**, e209 (2014).
28. Mehlhorn, U., Geissler, H. J., Laine, G. A. & Allen, S. J. Myocardial fluid balance. *Eur. J. Cardiothorac. Surg.* **20**, 1220–1230 (2001).
29. Friedrich, M. G. Myocardial edema–a new clinical entity? *Nat. Rev. Cardiol.* **7**, 292–296 (2010).
30. Li, X. et al. Inhibition of fatty acid oxidation enables heart regeneration in adult mice. *Nature* **622**, 619–626 (2023).
31. Yu, H. et al. LARP7 protects against heart failure by enhancing mitochondrial biogenesis. *Circulation* **143**, 2007–2022 (2021).
32. Zhang, Y. S. et al. Bioenergetic metabolism modulatory peptide hydrogel for cardiac protection and repair after myocardial infarction. *Adv. Funct. Mater.* **12**, 2312772 (2024).
33. Zhang, N. et al. Biomimetic and NOS-responsive nanomotor deeply delivery a combination of MSC-EV and mitochondrial ROS scavenger and promote heart repair and regeneration. *Adv. Sci.* **10**, e2301440 (2023).
34. Saunders, T. L. et al. Exposure of the inner mitochondrial membrane triggers apoptotic mitophagy. *Cell Death Differ.* **31**, 335–347 (2024).
35. Chen, G. et al. Structural basis for recognition of N-formyl peptides as pathogen-associated molecular patterns. *Nat. Commun.* **13**, 5232 (2022).
36. Morris, G., Gevezova, M., Sarafian, V. & Maes, M. Redox regulation of the immune response. *Cell Mol. Immunol.* **19**, 1079–1101 (2022).
37. Bhattacharyya, S. & Tobacman, J. K. SARS-CoV-2 spike protein-ACE2 interaction increases carbohydrate sulfotransferases and reduces N-acetylgalactosamine-4-sulfatase by p38 MAPK. *Signal Transduct. Target Ther.* **9**, 39 (2024).
38. Frangogiannis, N. G. Cardiac fibrosis. *Cardiovasc. Res* **117**, 1450–1488 (2021).
39. Frangogiannis, N. G. & Kovacic, J. C. Extracellular matrix in ischemic heart disease, part 4/4: JACC focus seminar. *J. Am. Coll. Cardiol.* **75**, 2219–2235 (2020).
40. Jin, A., Wang, Y., Lin, K. & Jiang, L. Nanoparticles modified by polydopamine: Working as "drug" carriers. *Bioact. Mater.* **5**, 522–541 (2020).
41. Zhang, M. et al. Sequential therapy for bone regeneration by cerium oxide-reinforced 3D-printed bioactive glass scaffolds. *ACS Nano* **17**, 4433–4444 (2023).
42. Wang, S. et al. Energy-supporting enzyme-mimic nanoscaffold facilitates tendon regeneration based on a mitochondrial protection and microenvironment remodeling strategy. *Adv. Sci.* **9**, e2202542 (2022).
43. Huang, Q. et al. Passively-targeted mitochondrial tungsten-based nanodots for efficient acute kidney injury treatment. *Bioact. Mater.* **21**, 381–393 (2023).
44. Zhang, Y. et al. The long noncoding RNA lncCIRBIL disrupts the nuclear translocation of Bclaf1 alleviating cardiac ischemia-reperfusion injury. *Nat. Commun.* **12**, 522 (2021).
45. Zhang, W. et al. AIE-enabled transfection-free identification and isolation of viable cell subpopulations differing in the level of autophagy. *Autophagy* **19**, 3062–3078 (2023).

Acknowledgements

This project was supported by the Major Project of Natural Science Foundation of Hunan Province (Open Competition) (No. 2021JC0002), National Key Research and Development Program of China (No. 2020YFC2008002), National Natural Science Foundations of China (No. 82325006, No. 82373871, No. 82270446, 81822004, 81974508, 82001486, and 21974134), Science and Technology Innovation Program of Hunan Province (No. 2020RC4006), Hunan Science Fund for Distinguished Young Scholar of China (No. 2021JJ10067), National Science Foundation of Hunan (No. S2022JJQNJJ2181 and 2020SK1013), Project of Innovation-driven Plan in Central South University (No. 2020CX017), Innovation-Driven Project of Central South University (202045005), Central South University Research Programme of Advanced Interdisciplinary Studies (2023QYJC017), Key Research and Development Program of Hunan Province (2024JK2114) and Key Research Project of Ningxia Hui Autonomous Region of China (Major Project) (No. 2023BEG02038). The authors thank Luo Song, Yilong Guo, and Hao Yu for their professional comments on grammar usage, narration, and constructive advice on figure descriptions; Hongqing Ma, Xiaohui Gong, and Jian Zhang for assistance in experiment.

Author contributions

Y.B. and K.A. conceived the project and designed the experiments. Y.L. and S.W. performed the majority of the experiments and wrote the manuscript. J.Z. and Q.S. made important intellectual contributions and helped revise the manuscript. Y.X., J.C., M.Y., G.Z., Q.H, T.Z, Q.H, X.S., and C.F. performed experiments and/or provided research assistance.

Competing interests

The authors declare no competing interests.

Additional information

Supplementary information The online version contains supplementary material available at https://doi.org/10.1038/s41467-024-50854-4.

Correspondence and requests for materials should be addressed to Kelong Ai or Yongping Bai.

Peer review information *Nature Communications* thanks Lina Ghibelli, and the other, anonymous, reviewer(s) for their contribution to the peer review of this work. A peer review file is available.